Quasar lifetime measurements from extended Lyα nebulae at z ~ 6

Ďurovčíková, D.; Eilers, A.-C.; Meyer, R.A.; Farina, E.P.; Bañados, E.; Davies, F.B.; ... ; Walter, F.

The Astrophysical Journal, 990:174 (12pp), 2025 September 10 https://doi.org/10.3847/1538-4357/adf6dd

Quasar Lifetime Measurements from Extended Lyα Nebulae at $z \sim 6$

Dominika Ďurovčíková[1,2], Anna-Christina Eilers[1,2], Romain A. Meyer[3], Emanuele Paolo Farina[4], Eduardo Bañados[5], Frederick B. Davies[5], Joseph F. Hennawi[6,7], Chiara Mazzucchelli[8], Robert A. Simcoe[1,2], and Fabian Walter[5]
[1] MIT Kavli Institute for Astrophysics and Space Research, 77 Massachusetts Avenue, Cambridge, MA 02139, USA; dominika@mit.edu
[2] Department of Physics, Massachusetts Institute of Technology, 77 Massachusetts Avenue Cambridge, MA 02139, USA
[3] Department of Astronomy, University of Geneva, Chemin Pegasi 51, 1290 Versoix, Switzerland
[4] International Gemini Observatory/NSF NOIRLab, 670 N A'ohoku Place, Hilo, HI 96720, USA
[5] Max Planck Institut für Astronomie, Königstuhl 17, D-69117, Heidelberg, Germany
[6] Leiden Observatory, Leiden University, P.O. Box 9513, 2300 RA Leiden, The Netherlands
[7] Department of Physics, University of California, Santa Barbara, CA 93106, USA
[8] Instituto de Estudios Astrofísicos, Facultad de Ingeniería y Ciencias, Universidad Diego Portales, Avenida Ejercito Libertador 441, Santiago, Chile
Received 2025 April 25; revised 2025 July 7; accepted 2025 July 24; published 2025 September 8

Abstract

The existence of billion-solar-mass black holes hosted in luminous quasars within the first gigayear of cosmic history poses a challenge to our understanding of supermassive black hole (SMBH) growth. The problem is further exacerbated by the very short quasar lifetimes of $t_Q \lesssim 10^6$ yr, as derived from the extent of their proximity zone (PZ) sizes observed in the quasars' rest-UV spectra. However, the quasar lifetime estimates based on the extents of the PZs may be underestimated, as time-variable obscuration effects might have limited the quasars' emission along our sightline in the past. In this work, we present independent quasar lifetime measurements for six quasars at $z \sim 6$ leveraging the extended nebular emission perpendicular to our line of sight. We use observations from the Very Large Telescope/Multi-Unit Spectroscopic Explorer to search for extended Lyα emission in the circumgalactic medium around quasars with small PZs and estimate their lifetimes as the light travel time between the SMBH and the outer edge of the nebula. We find agreement between the independent lifetime estimates. For one object we find a proximate absorption system prematurely truncating the extent of the quasar's PZ, which thus results in an expected discrepancy between the lifetime estimates. Our results provide further evidence that the quasars' current accretion episode has only recently begun, challenging our models of SMBH growth.

Unified Astronomy Thesaurus concepts: Quasars (1319); Supermassive black holes (1663); Nebulae (1095); Circumgalactic medium (1879); Early universe (435)

1. Introduction

The growth of supermassive black holes (SMBHs) through accretion is accompanied by the release of copious amounts of radiation (A. Soltan 1982; Q. Yu & S. Tremaine 2002), enabling their observation as quasars out to high redshifts (X. Fan et al. 2023). However, the discovery of billion-solar-mass black holes (BHs) hosted in quasars at $z \gtrsim 6$ (e.g., X.-B. Wu et al. 2015; E. Bañados et al. 2018; F. Wang et al. 2020, 2021) presents a significant challenge to standard BH growth models. Even under the assumption of continuous, Eddington-limited accretion, growing an SMBH from a $100\,M_\odot$ seed to a billion solar masses would require nearly 1 billion yr (K. Inayoshi et al. 2020). This timescale is comparable to the age of the Universe at these redshifts.

Maintaining such steady growth is challenging for many reasons, e.g., due to disruptions from BH feedback and supernova explosions (e.g., J. L. Johnson & V. Bromm 2007; D. Whalen et al. 2008; Y. Zhou et al. 2024). A variety of alternative pathways have thus been proposed to allow a more rapid BH mass build-up over cosmic time, such as episodic accretion with phases of obscured growth and/or super-Eddington accretion (F. B. Davies et al. 2019; S. Satyavolu et al. 2023a), growth driven by BH mergers (e.g., M. Volonteri & M. J. Rees 2006; T. Tanaka & Z. Haiman 2009), or jet-assisted growth (T. Connor et al. 2024).

The problem gets even more severe as high-redshift quasars appear to have only been active for a short amount of time. Short UV-luminous quasar lifetimes have been measured at $z \sim 6$ primarily from proximity zones (PZs), the regions of increased transmission blueward of Lyα carved out into the intergalactic medium (IGM) by the quasars' ionizing radiation. Considering the balance of photoionization and recombination timescales for a hydrogen-rich IGM, A.-C. Eilers et al. (2017) used radiative transfer simulations to establish a relation between Lyα PZ sizes and quasar lifetimes. Since then, such measurements of PZ sizes (A.-C. Eilers et al. 2017, 2018, 2020, 2021; K. A. Morey et al. 2021; S. Satyavolu et al. 2023b), as well as the modeling of damping wings (F. B. Davies et al. 2019; D. Ďurovčíková et al. 2024), have revealed a population of quasars with surprisingly small PZs that imply lifetimes of $t_Q \lesssim 10^6$ yr. These short SMBH growth timescales at $z \sim 6$ have been supported by independent measurements of quasar duty cycles from clustering measurements (A.-C. Eilers et al. 2024; E. Pizzati et al. 2024).

Interestingly, one way to alleviate the tension between the long BH growth timescales required by Eddington-limited accretion and the short timescales implied by quasar lifetime measurements at $z \sim 6$ is if time-variable, sightline-dependent obscuration effects are present (F. B. Davies et al. 2019; S. Satyavolu et al. 2023a). If luminous high-redshift quasars indeed underwent a significant portion of their SMBH growth

Table 1
The Quasar Sample Used in This Study

Quasar	R.A. (hh:mm:ss.ss)	Decl. (dd:mm:ss.s)	Redshift	M_{1450}[a] (mag)	R_p[b] (pMpc)	$\log t_Q$[c] (yr)	References[d]	Total Exp. Time (s)
PSO J004+17	00:17:34.47	+17:05:10.7	5.8166	−26.01	1.16 ± 0.15	$3.6^{+0.5}_{-0.4}$	E21	14090
SDSS J0100+2802	01:00:13.02	+28:02:25.8	6.3270	−29.14	7.12 ± 0.13	$5.1^{+1.3}_{-0.7}$	D20	12681
VDES J0330–4025	03:30:27.92	−40:25:16.2	6.249	−26.42	$1.69^{+0.62}_{-0.35}$	$4.1^{+1.8}_{-0.9}$	E21	14090
PSO J158–14	10:34:46.51	−14:25:15.9	6.0685	−27.41	1.95 ± 0.14	$3.8^{+0.4}_{-0.3}$	E21	30540
CFHQS J2100–1715[e]	21:00:54.62	−17:15:22.5	6.0806	−25.55	0.37 ± 0.15	2.3 ± 0.7	E21	13338
CFHQS J2229+1457	22:29:01.65	+14:57:09.0	6.1517	−24.78	0.47 ± 0.15	$2.9^{+0.8}_{-0.9}$	E21	16908

Notes. All errors are 1σ errors.
[a] The absolute magnitude at rest frame 1450 Å.
[b] The PZ size.
[c] The quasar lifetime based on the PZ size.
[d] The reference from which the redshift, R_p, and t_Q measurements are adopted. Note that all redshifts are from [C II] observations, except for VDES J0330–4025, whose redshift is Mg II based while accounting for the Mg II-[C II] systematic shift. E21—A.-C. Eilers et al. (2021); D20—F. B. Davies et al. (2020).
[e] Deep MUSE observations of this quasar have been previously analyzed by A. B. Drake et al. (2019) and E. P. Farina et al. (2019). We include this data in our study for completeness.

in a partially obscuring medium, the UV emission along some sightlines could have been limited in the past, thus potentially imprinting smaller PZs or stronger damping wings in the observed spectra of these quasars (F. B. Davies et al. 2019). Likewise, the short quasar duty cycles measured via clustering studies of UV-luminous quasars at $z \sim 6$ could be explained if the fraction of obscured quasars in the early Universe is high (A.-C. Eilers et al. 2024).

To investigate the role that obscured growth plays in the assembly of these early SMBHs, we apply an alternative method to measure quasar lifetimes at high redshifts that is sensitive to the quasar's emission in the direction perpendicular to our line of sight. This method relies on the imprints of quasars' radiation on a much smaller (∼kpc) spatial scale compared to the PZs (∼Mpc), namely, on the extended nebular emission of the gas inside the circumgalactic medium (CGM) around the quasar. Assuming that this nebular glow is powered by the quasar's radiation, which has been shown to be the case at least for the brightest nebulae (S. Cantalupo et al. 2014; E. Borisova et al. 2016b; T. Costa et al. 2022), the quasar lifetime is measured as the light travel time between the quasar and the outer edge of the nebula. Such a measurement relies on a fundamentally different physical mechanism than PZ-based lifetimes (i.e., light travel timescale versus hydrogen recombination timescale) and thus constitutes an independent measurement of quasar ages. This method has been previously applied to quasars at lower redshifts (R. Trainor & C. C. Steidel 2013; S. Cantalupo et al. 2014; J. F. Hennawi et al. 2015; E. Borisova et al. 2016a), but such extended nebular emission has been found to be ubiquitous around quasars across cosmic time (e.g., T. M. Heckman et al. 1991a, 1991b; L. Christensen et al. 2006; J. F. Hennawi & J. X. Prochaska 2013; S. Cantalupo et al. 2014; D. C. Martin et al. 2014; F. Arrigoni Battaia et al. 2016; E. Borisova et al. 2016b; E. P. Farina et al. 2017, 2019; A. B. Drake et al. 2019).

In this work, we use deep (>3.5 hr) observations with the Very Large Telescope/Multi-Unit Spectroscopic Explorer (MUSE; R. Bacon et al. 2010) to measure nebular lifetimes of a sample of $z \sim 6$ quasars with small PZs and thus short inferred lifetimes of $t_Q \lesssim 10^6$ yr (some of which are as low as $t_Q \sim 10^3$ yr; A.-C. Eilers et al. 2020, 2021; M. Yue et al. 2023). We chose this sample for two reasons. First, the extremely short PZ-based lifetimes of these high-redshift quasars, taken together with their measured single-epoch BH masses, pose the greatest challenge to our understanding of SMBH assembly. Second, because the growth of ionized nebulae is limited by the speed of light (see Appendix A) and the ionizing photon flux decays as $\sim 1/r^2$ away from the quasar, these young quasars should be surrounded by nebulae that are small enough to measure their true extent above the noise level. Notably, E. P. Farina et al. (2019) and A. B. Drake et al. (2019) have found an intriguing nondetection of a Lyα nebula in a deep (3.7 hr) observation of the $z \sim 6$ quasar CFHQS J2100–1715 that exhibits a small PZ corresponding to a lifetime of $t_Q \lesssim 10^3$ yr, as well as two more nondetections in shallower observations of quasars with short PZ-based lifetimes, SDSS J0100+2802 and CFHQS J2229+1457. Our study aims to explore this result further and establish whether these quasars have indeed only recently begun their accretion activity, showing only very small (or no) extended nebular emission, or whether very extended nebulae are present, which would point toward sightline-dependent obscuration effects as the cause for the small observed PZs.

We first describe the data set in Section 2 and subsequently explain how we search for Lyα nebulae in Section 3. In Section 4, we explain the details of the nebular lifetime measurement. Finally, we discuss the comparison to the previously published, PZ-based lifetimes for our quasar sample as well as the implications of our results in Section 5. Throughout this paper, we use the flat ΛCDM cosmology with $h = 0.67$, $\Omega_M = 0.31$, $\Omega_\Lambda = 0.69$ (Planck Collaboration et al. 2020).

2. Data

2.1. Sample of Young z ∼ 6 Quasars

In order to investigate the implications of short PZ-based lifetimes on SMBH growth, we focus on a sample of quasars that have been previously reported to have small PZs and short inferred lifetimes that are unaffected by gravitational lensing (A.-C. Eilers et al. 2020, 2021; M. Yue et al. 2023). Detailed information on this sample is shown in Table 1.

For our search of extended Lyα emission, we use archival observations from the VLT/MUSE integral-field spectrograph (R. Bacon et al. 2010) in the Wide Field Mode with natural seeing (WFM-noAO). All objects in our sample have deep (>3.5 hr) observations, which is important when searching for the faint extended emission. PSO J158–14 and VDES J0330–4025 were observed between 2020 November and 2021 March under program 106.215A (PI: Eilers). PSO J004+17 was observed between 2021 November and 2022 September under program 108.222J (PI: Eilers). For SDSS J0100+2802, we combine observations from program 108.222J (PI: Eilers, observed in 2021 October and November) and 0101.A-0656 (PI: Farina, observed in 2018 August). Observations of CFHQS J2229+1457 are combined from program 108.222J (PI: Eilers, observed between 2021 October and 2022 August) and 0103.A-0562 (PI: Farina, observed in July 2019).[9] Observations of CFHQS J2100–1715 come from 2016 August (program 297.A-5054, PI: Decarli) and have been analyzed before by A. B. Drake et al. (2019) and E. P. Farina et al. (2019). We choose to reanalyze the last quasar here for completeness and for consistency with the rest of our sample. The total exposure times for individual quasars are listed in Table 1.

2.2. Data Reduction

The data used in this study were reduced using the MUSE Data Reduction Software (P. M. Weilbacher et al. 2012, 2014), which performs bias subtraction, flat-fielding, twilight and illumination corrections, and applies wavelength and flux calibration using standard stars. For CFHQS J2100–1715, we use the same archival observations as well as reduction pipeline as in E. P. Farina et al. (2019) and A. B. Drake et al. (2019). Note that on top of the standard reduction pipeline (v2.6), E. P. Farina et al. (2019) implement a number of custom steps, including improvements to flat-fielding and sky subtraction, and a custom absolute flux calibration and astrometry solution. The rest of the observations of our quasar sample were reduced using v2.8.7 of the MUSE pipeline with standard parameters. As voxel-to-voxel correlations may lead to underestimated noise properties of the thus reduced data cubes (R. Bacon et al. 2015), we rescaled all variance data cubes to match the measured variance of the background (E. Borisova et al. 2016b; E. P. Farina et al. 2017, 2019; F. Arrigoni Battaia et al. 2019). In all cases, the reduced data cubes were further run through the Zurich Atmospheric Purge code (ZAP; K. T. Soto et al. 2016) to further clean the sky line emission. For the subsequent analysis, we use the ZAP-ped data cubes as they are cleaner from artifacts, which is crucial for our search for faint extended line emission.

3. Uncovering Lyα Nebulae

In this section, we describe the analysis pipeline used to search for extended Lyα emission around the quasars in our sample. This procedure is primarily based on the methods used in the REQUIEM survey (E. P. Farina et al. 2019) with a few differences on which we elaborate below.

We first cut the data cubes to $14'' \times 14''$ around the quasar (corresponding to 80 pkpc × 80 pkpc at $z \sim 6$) to ease computation in subsequent steps. We then mask foreground sources using emission blueward of the Lyα wavelength of the quasar where most of the quasar radiation is suppressed due to the IGM (J. E. Gunn & B. A. Peterson 1965). We perform this step by collapsing the data cube in the foreground of the quasar's Lyα emission and searching for emission above a signal-to-noise ratio (SNR) threshold (ranging from 2 to 10 depending on the specific quasar field) to pick out obvious sources (omitting any residual transmission of the quasar itself). The foreground here is defined to lie between 6000 Å in the observed frame and the wavelength corresponding to 5× the PZ size blueward of Lyα (as given by Table 1; see Appendix B).

We proceed by masking spectral channels with large surface brightness uncertainty, strong sky line emission, or residual detector artifacts. To remove high-uncertainty channels, we use the variance extension of the data cube and mask spectral channels with outlying overall uncertainty. As for the latter two, elevated background is a telltale sign of channels with sky line emission or residual artifacts. We remove these by calculating the background in an annular aperture at a radius comparable to the size of our cutout cube, and we mask spectral channels that show rapid departures from the smoothly varying sky background.

Subsequently, we perform point-spread function (PSF) extraction and subtraction using standard methods, summarized here briefly. We extract the PSF from the red wing of the Lyα line, which originates from the parsec-scale broad-line region (BLR) of the quasar and thus represents a true unresolved point source. Specifically, we collapse each data cube across a narrow wavelength range at 2500 km s^{-1} redward of the quasar Lyα line to create a narrowband image that constitutes our PSF model (displayed in the second panel from the left in Figures 1 and 2; see Appendix B for the exact spectral regions for each quasar). This wavelength region should thus be free of significant extended emission, assuming the host galaxy contribution is negligible at these redshifts in ground-based observations. With this PSF model at hand, we subtract it from each channel separately, channel-by-channel normalizing the model to the integrated flux inside an aperture with a radius of 0.″4 centered on the quasar (middle panel in Figures 1 and 2).

As the last step, we use the PSF-subtracted cube to search for extended Lyα emission around the quasar. We first compute a smoothed cube, following J. F. Hennawi & J. X. Prochaska (2013), F. Arrigoni Battaia et al. (2015), and E. P. Farina et al. (2017, 2019):

$$\mathrm{SMOOTH}[\chi_{x,y,\lambda}] = \frac{\mathrm{CONVOL}[\mathrm{DATA}_{x,y,\lambda} - \mathrm{PSF}_{x,y,\lambda}]}{\sqrt{\mathrm{CONVOL}^2[\sigma^2_{x,y,\lambda}]}}, \quad (1)$$

where $\mathrm{DATA}_{x,y,\lambda}$ represents the data cube, $\mathrm{PSF}_{x,y,\lambda}$ is the aforementioned three-dimensional PSF model normalized at each spectral channel, and $\sigma^2_{x,y,\lambda}$ represents the variance data cube. The CONVOL operation denotes a convolution with a three-dimensional Gaussian kernel with $\sigma_{x,y} = 0.''2$ in the spatial direction and $\sigma_\lambda = 2.5$ Å in the spectral direction (same as in E. P. Farina et al. 2019). The thus constructed $\mathrm{SMOOTH}[\chi_{x,y,\lambda}]$ is essentially a smoothed SNR cube (pseudonarrowband images of $\chi_{x,y,\lambda}$ and $\mathrm{SMOOTH}[\chi_{x,y,\lambda}]$ are shown in the two rightmost panels in Figures 1 and 2).

Identifying the extended nebular emission requires us to search the $\mathrm{SMOOTH}[\chi_{x,y,\lambda}]$ cube for groups of connected

[9] Note that some of the observations (<1 hr) of SDSS J0100+2802 and CFHQS J2229+1457 were previously a part of the REQUIEM survey (E. P. Farina et al. 2019) and yielded no nebular detections.

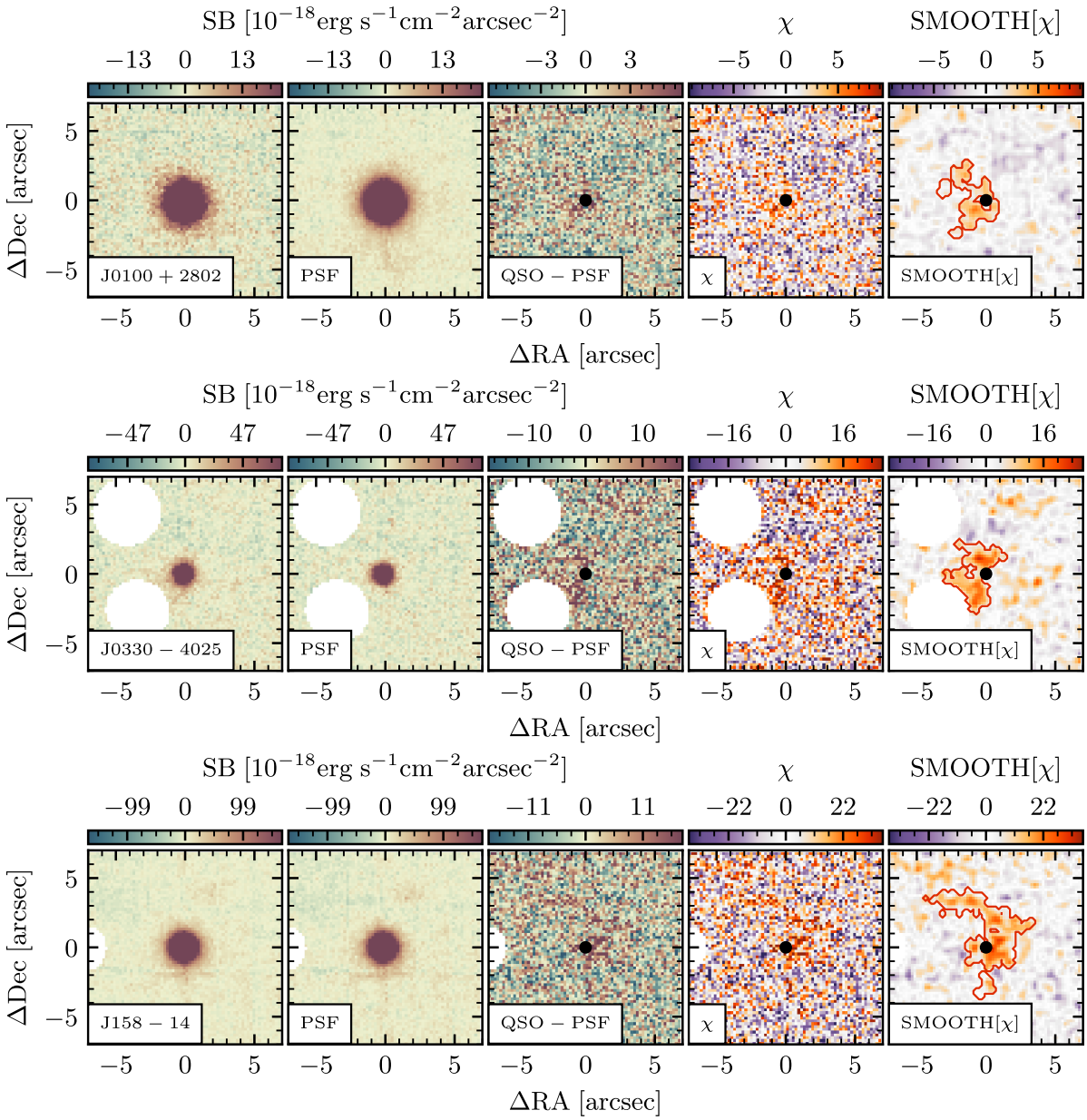

Figure 1. Quasars in our sample with extended nebular emission. From left to right, the panels display pseudonarrowband images of (1) the quasar's emission around Lyα, (2) the PSF extracted from the broad wing of the quasar's Lyα line, (3) the PSF-subtracted data, (4) the χ data, essentially representing the SNR of the PSF-subtracted data, and (5) the smoothed χ data showing the extended nebular emission. Panels (1), (3), (4), and (5) are collapsed across the wavelength range of the detected nebula, and panel (2) is collapsed across the wavelength range of the PSF extraction, as displayed in Appendix B. White patches correspond to masked foreground sources.

voxels that contain significant line emission and thus to construct a 3D mask of the nebula. We perform this search by first finding the most significant voxel in a 1000 km s^{-1} spectral window around Lyα and at most 1″ away from the quasar. Once this voxel is identified, we run a friends-of-friends algorithm to link up all voxels that (i) have a significance above a certain $\mathrm{SNR}_{\mathrm{thres}}$ and (ii) are within a linking distance $l_{\mathrm{thres},x,y}$ in the spatial direction and within $l_{\mathrm{thres},\lambda}$ in the spectral direction. Additionally, we impose that a group has to contain more than 100 linked voxels to be considered a nebula.[10]

To explore the robustness of the size of the nebulae, we repeated the linking procedure using the following combination of linking thresholds: $\mathrm{SNR}_{\mathrm{thres}} = \{2.0, 3.0\}$, $l_{\mathrm{thres},x,y} = \{0\farcs4, 0\farcs6\}$, and $l_{\mathrm{thres},\lambda} = \{2.5\text{Å}, 3.75\text{Å}\}$ (corresponding to a linking length of 2 and 3 spatial and spectral pixels, respectively). Using the resultant 3D nebular masks, we computed a median mask of the nebula for each quasar, which we use in Figures 1 and 3.

We detect extended Lyα emission in three quasars in our sample (shown in Figure 1), while the remaining three do not exhibit any nebula above the noise level (Figure 2). We further measured the surface brightness limits for all six quasars by collapsing each data cube across five wavelength channels centered at the quasar's Lyα emission and measuring the

[10] For a cylinder with a base radius of 1″, 100 voxels corresponds to a height of 55 km s^{-1} centered at Lyα at $z = 6$.

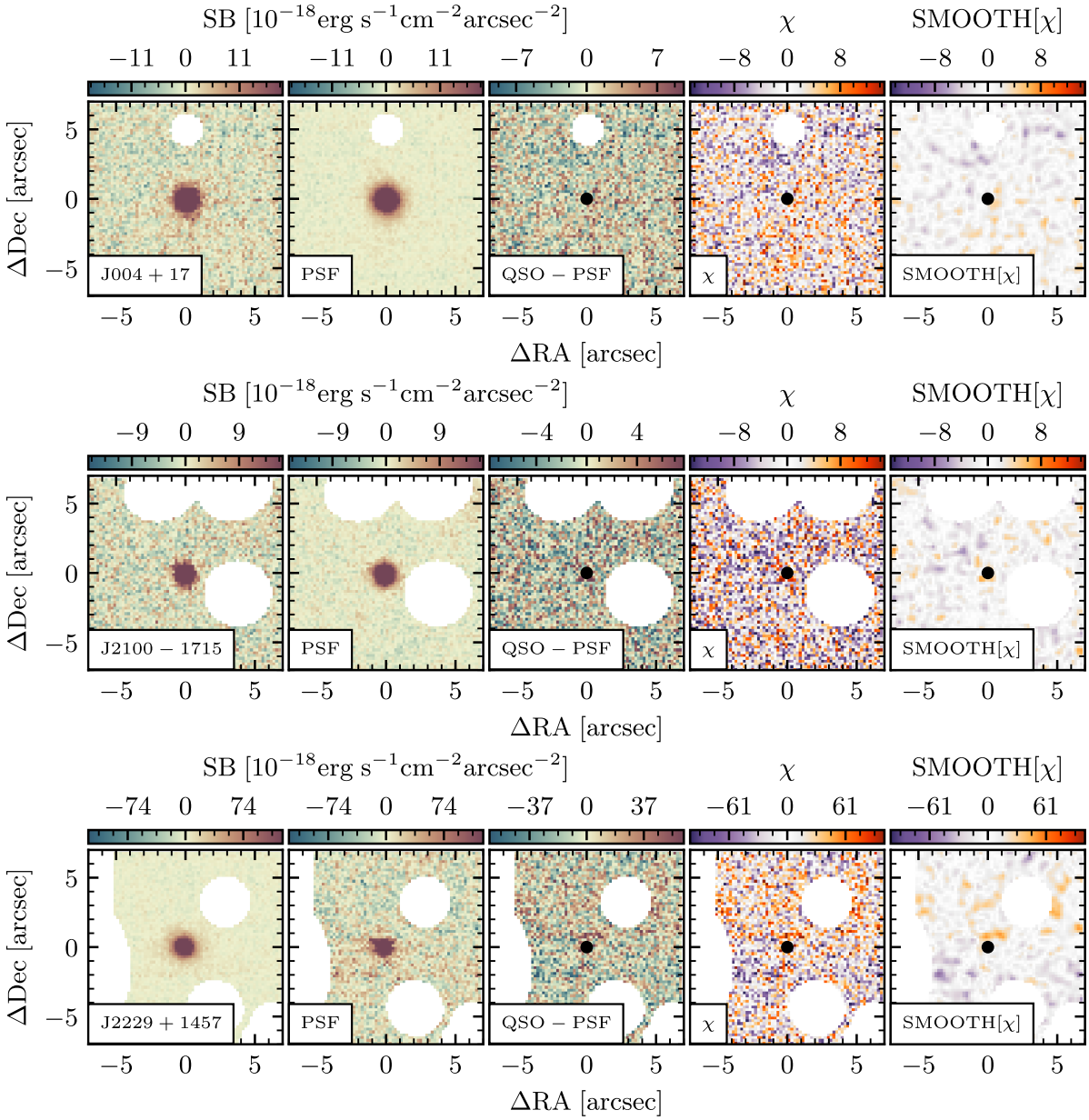

Figure 2. Quasars in our sample without a nebular detection. Panels are the same as in Figure 1, but panels (1), (3), (4), and (5) are now collapsed in a 1000 km s^{-1} spectral window around the quasar's Lyα emission.

variance in a 1arcsec^2 aperture, following the literature (e.g., E. P. Farina et al. 2017, 2019). The measured 5σ limits are given in Table 2 and are comparable across all observations. This fact demonstrates that the nondetections are unlikely to be a consequence of a lack of sensitivity.

Additionally, in Figure 3 we visualize the velocity structure in the detected nebulae. We constructed the channel maps shown in the left part of the figure as follows. For each detection, we measured the maximum velocity offset in the nebular mask. We then divided the velocity range defined by this offset into three spectral channels of equal widths (766 km s^{-1} for J0330–4025, 946 km s^{-1} for J158–14, and 420 km s^{-1} for J0100+2802), such that the second spectral channel is centered on the quasar's Lyα emission. Within each channel, we color-coded each nebular voxel by its velocity offset from the Lyα emission of each quasar. Note that despite the large velocity range of all three nebulae, the channel centered on the quasar rest frame encompasses the maximum transverse distance between the quasar and the edge of extended emission, except in the case of J0100+2802 whose nebula is overall blueshifted by ~-400 km s^{-1}.

Additionally, we extracted the integrated line profile of each median nebula, shown in the right part of Figure 3. We used the nebular line profiles to measure the velocity range, $\Delta v^{\mathrm{Ly}\,\alpha}$, and the velocity dispersion, $\sigma_v^{\mathrm{Ly}\alpha}$, for each quasar (Table 2). The properties of the detected nebulae are comparable to nebulae found in large surveys in the literature (E. Borisova et al. 2016b; E. P. Farina et al. 2019).

4. Quasar Lifetime Measurements Based on the Extended Lya Nebular Emission

With the nebular (non)detections at hand, we proceed to measure the nebular quasar lifetimes, $t_{\mathrm{Q}}^{\mathrm{Ly}\alpha}$. Assuming that the extended nebular emission is powered primarily by the

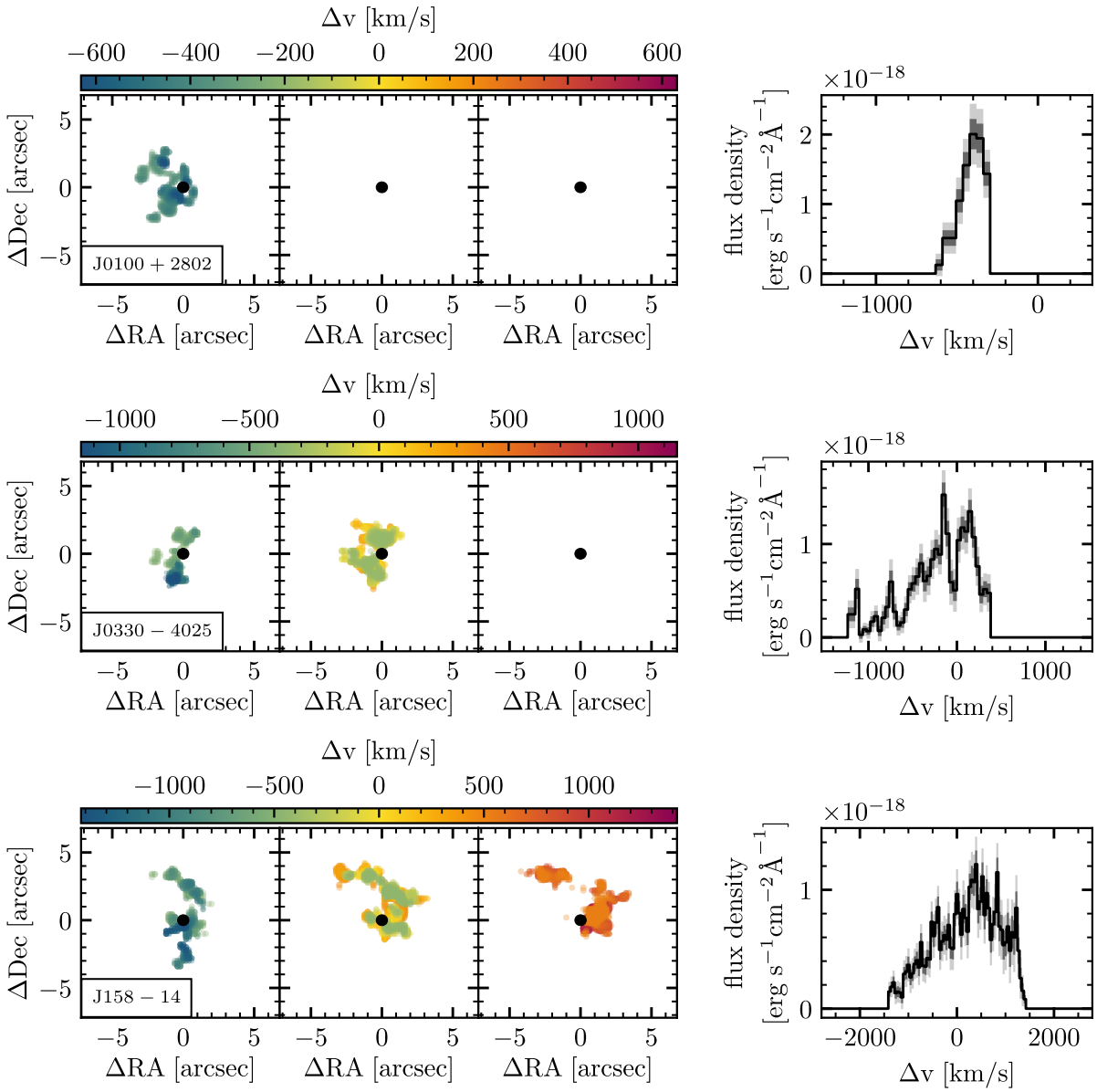

Figure 3. Spectral decomposition of the three nebular detections. The left three panels display the detected nebulae in three spectral channels of equal widths (766 km s^{-1} for J0330–4025, 946 km s^{-1} for J158–14, and 420 km s^{-1} for J0100+2802), whereby the middle panel is centered on the quasar's systemic redshift, as given by Table 1. We also color-code each displayed voxel by the velocity offset from the quasar's Lyα emission. The right panel shows the integrated emission line profile of the detected nebula.

Table 2
The Maximum Extent as well as Quasar Lifetime Measurements from the Extended Lyα Emission

Quasar	$SB^{L}_{5\sigma,Ly\alpha}$ [erg s^{-1} cm^{-2} arcsec^{-2}]	$\Delta v^{Ly\alpha}$ (km s^{-1})	$\sigma_v^{Ly\alpha}$ (km s^{-1})	$d_{max}^{Ly\alpha}$ (pkpc)	$\log t_Q^{Ly\alpha}$ (yr)
PSO J004+17	2.9×10^{-18}	...	...	<2.37	<3.89
SDSS J0100+2802	6.5×10^{-18}	273^{+1692}_{-63}	70^{+471}_{-11}	$17.92^{+3.58}_{-3.58}$	$4.77^{+0.08}_{-0.10}$
VDES J0330–4025	3.8×10^{-18}	793^{+775}_{-738}	184^{+187}_{-184}	$8.36^{+22.83}_{-6.08}$	$4.44^{+0.57}_{-0.56}$
PSO J158–14	3.8×10^{-18}	2333^{+458}_{-765}	581^{+85}_{-164}	$23.85^{+23.70}_{-9.17}$	$4.89^{+0.30}_{-0.21}$
CFHQS J2100–1715	2.9×10^{-18}	...	...	<2.32	<3.88
CFHQS J2229+1457	4.4×10^{-18}	...	...	<2.30	<3.88

Note. The uncertainties correspond to the 16th and 84th percentiles of the distribution of $d_{max}^{Ly\alpha}$ and $\log t_Q^{Ly\alpha}$.

quasar's radiation (e.g., S. Cantalupo et al. 2014; E. Borisova et al. 2016b; T. Costa et al. 2022), we calculate the quasar lifetime as the light travel time between the quasar and the outer edge of the nebula in the transverse direction. Such calculation only holds in the regime where the size of the nebula grows at or close to the speed of light, which, as we

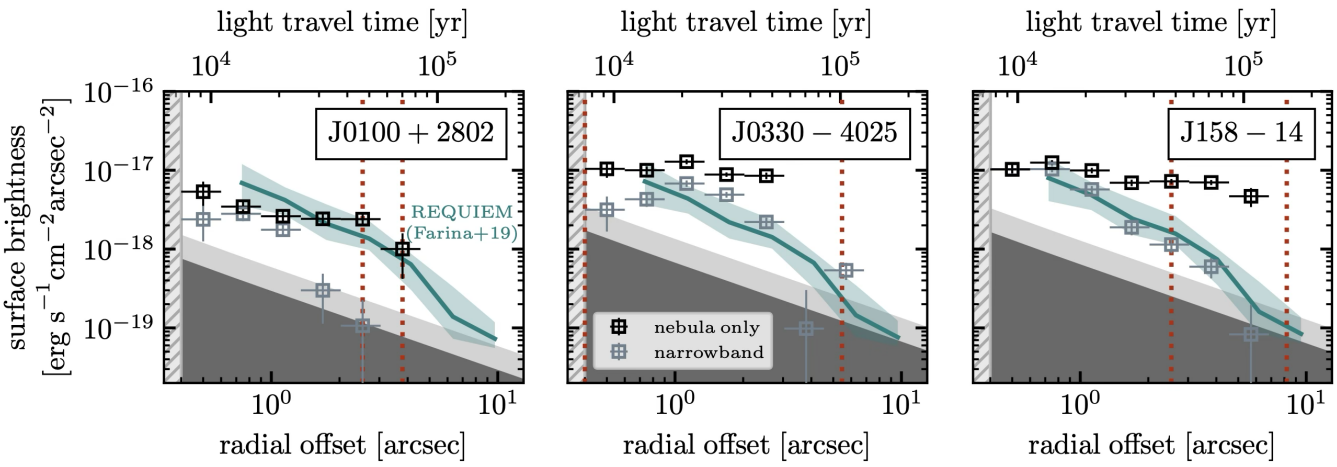

Figure 4. The extracted surface brightness profiles for the three quasars with nebular detections as a function of both the radial offset and the light travel time from the quasar. The black data points correspond to the surface brightness profile of the median nebula, as described in Section 3, where we only take into account the nebular pixels so as not to dilute signal at the edge of the nebula. We also show the surface brightness profile calculated via annular averaging of the full narrowband image of the detected nebula as gray data points to illustrate this signal dilution. In the background, we display the median stacked surface brightness profile of $z > 5.7$ quasars from E. P. Farina et al. (2017) for comparison. The red dotted lines display the 16th and 84th percentile spread of the nebular extent when the nebular search parameters are varied. The quasar lifetime, $t_{\rm Q}^{{\rm Ly}\alpha}$, is measured as the light travel time from the quasar to the outer edge of the detected nebula in the transverse direction. Note that the horizontal error bars represent the binning of the annular apertures used to calculate the surface brightness. We also display the 1σ (dark gray) and 2σ (light gray) background derived from the sky variance in the outermost annular aperture.

show in Appendix A, is valid for lifetimes of at least up to $t_{\rm Q}^{{\rm Ly}\alpha} \sim 10^5$ yr for typical CGM densities.

In order to determine the extent of each nebula, we first compute its surface brightness profile. We collapse the PSF-subtracted data cube across the wavelength range of the detected nebular emission and use this pseudonarrowband image of the nebula to perform aperture sum in annular regions centered on the quasar at increasing radii. We choose annular apertures at logarithmically increasing radii, starting at a separation of $0\farcs4$ away from the quasar—this is to avoid contamination by the region that was used to normalize the PSF model at each wavelength channel. Because we are interested in measuring the maximum extent of the nebula, we only apply the aperture sum on the voxels contained in the nebular mask to avoid diluting the signal at the outskirts of the nebula. This is in contrast to computing the aperture sum within the whole annulus irrespective of the nebular mask, as is done elsewhere in the literature, e.g., E. Borisova et al. (2016b) and E. P. Farina et al. (2019), which leads the surface brightness profile to smoothly approach the background noise. This difference is illustrated in Figure 4 for the three nebular detections in our sample, where we show both the nebula-only surface brightness profiles (in black) alongside the full surface brightness profiles (in gray; the difference is also nicely illustrated in, e.g., F. Arrigoni Battaia et al. 2019). Additionally, we show the median surface brightness stack from the REQUIEM survey (E. P. Farina et al. 2019), scaled to the relevant quasar redshift, in the background as a teal curve. We also display the background surface brightness noise in gray, which we derive from the outermost annulus that does not include any nebular pixels. Note that the displayed surface brightness profiles are not corrected for cosmological dimming.

We identify the maximum extent of the nebula, $d_{\rm max}^{{\rm Ly}\alpha}$, based on the largest radius bin with a nebular detection (i.e., based on the black data points in Figure 4). We convert this radius from angular units to physical units via the angular diameter distance evaluated at the quasar redshift. Subsequently, we convert this maximum nebular extent to a lifetime measurement using the speed of light, c,

$$t_{\rm Q}^{{\rm Ly}\alpha} = \frac{d_{\rm max}^{{\rm Ly}\alpha}}{c}. \quad (2)$$

Note that $d_{\rm max}^{{\rm Ly}\alpha}$ here is the distance to the furthest point as projected onto the sky, as opposed to the furthest point in the three-dimensional space in the nebula. The transverse (projected) distance is the relevant quantity for this measurement as position and velocity information along the line of sight are difficult to disentangle—this is due to peculiar velocities boosting and/or broadening the Lyα emission profile (i.e., the Finger of God and Doppler effects). Such motion does not bias the nebular extent, and hence the quasar lifetime, measured in the transverse direction.

As detailed in Section 3, we performed the nebula search using a range of thresholds for the SNR and the spatial and spectral linking lengths of individual voxels. We use all the thus-created nebular masks to measure a distribution of nebular extents and quasar lifetimes. We include their median measurements as well as the 16th and 84th percentile uncertainties in Table 2 and also show these as vertical dotted red lines in Figure 4. For the quasars in our sample without detected Lyα nebulae, we place an upper bound on their properties based on the spatial region we do not resolve in our analysis ($0\farcs4$). Note that the surface brightness limits given in Table 2, which are comparable across all observations included in our sample, suggest that these are true nondetections—in fact, even if the nebulae of these three quasars were $10\times$ fainter than our detections (R. Mackenzie et al. 2021), we would still expect to marginally detect them at this sensitivity.

5. Implications for SMBH Growth

We have presented new lifetime measurements for a sample of six quasars at $z \sim 6$ based on the spatial extent of their nebular Lyα emission in deep (>3.5 hr) MUSE observations

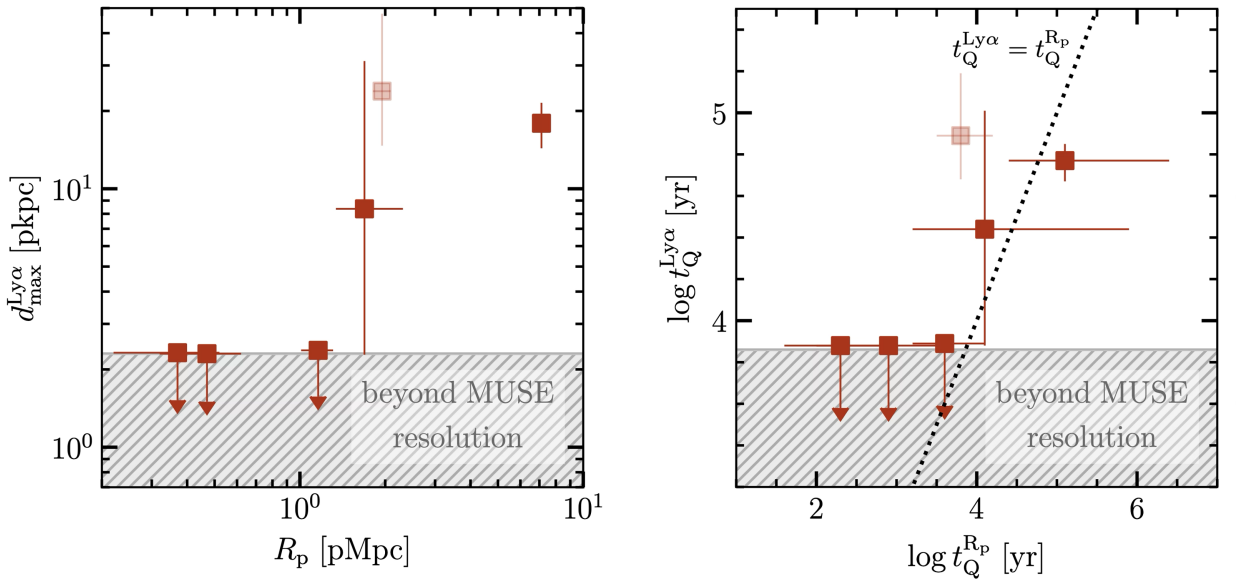

Figure 5. Left: a comparison of the newly measured Lyα nebula sizes, $d_{\rm max}^{\rm Ly\alpha}$, to the previously published PZ sizes of the quasars in our sample, from A.-C. Eilers et al. (2021) and F. B. Davies et al. (2020). Right: a comparison of the new quasar lifetimes derived from the sizes of Lyα nebulae, $t_{\rm Q}^{\rm Ly\alpha}$, to the existing PZ-based lifetimes, $t_{\rm Q}^{\rm R_P}$ (A.-C. Eilers et al. 2021; F. B. Davies et al. 2020). Correlations between the nebular and PZ-based quantities suggest that line-of-sight effects are likely not the cause of the short quasar lifetimes observed at high redshift. Indeed, we find agreement in the measured lifetimes for all quasars in our sample, except for one quasar, J158-14 (the faded data point), whose PZ is likely truncated by a proximate absorption system.

with comparable sensitivity. Three of these quasars exhibit extended Lyα emission, while the nebulae of the remaining three quasars remain undetected.

This quasar sample is particularly intriguing to study from the perspective of lifetimes as these quasars all exhibit extremely small PZs ($R_{\rm p}$) and thus very short PZ-based quasar lifetimes ($t_{\rm Q}^{\rm R_P}$, summarized in Table 1; F. B. Davies et al. 2020; A.-C. Eilers et al. 2020, 2021). A comparison between the sizes of the Lyα nebulae of these quasars, $d_{\rm max}^{\rm Ly\alpha}$, including the nondetections, and their PZs (shown in the left panel of Figure 5) suggests a correlation, meaning that line-of-sight effects and time-variable obscuration are unlikely the cause of these extremely small PZs. Indeed, our new nebular lifetime measurements (shown in the right panel of Figure 5) are also consistent with these short quasar lifetimes based on PZs. This is remarkable particularly because the two lifetime measurement methods are based on very different spatial scales (the kiloparsec-scale CGM vs the megaparsec-scale IGM) and very different physical mechanisms (light travel timescales vs ionization and recombination timescales) and thus constitute two truly independent measurements.

One of the quasars in our sample, J158–14, is shown as a faded data point in Figure 5. This is because, upon a closer inspection of the MUSE data, we identified a proximate Lyα emitter (LAE) that seems to be truncating the line-of-sight PZ of this quasar and thus results in an underestimate of the $t_{\rm Q}^{\rm R_P}$ measurement. This reconciles the tension between the two lifetime measurements for this quasar, whereby its nebular lifetime shows that this quasar is substantially older than its PZ seems to suggest. Coincidentally, this foreground LAE imparts no metal absorption lines on the spectrum of this quasar and is presented in a companion paper (D. Ďurovčíková et al. 2025).

The main caveats of these nebular lifetime measurements are as follows. First, we operate under the assumption that we are indeed seeing the edge of the nebula in the surface brightness profiles in Figure 4. Since we chose to compute our surface brightness profiles so as to avoid diluting the signal at the outskirts of the detected nebula, we would expect the surface brightness profiles to smoothly approach the background noise level if these observations were not sensitive enough to capture the full extent of the nebular emission. This is indeed supported by noticing that, in Figure 4, the full narrowband surface brightness profiles of J0100+2802 and J0330–4025[11] (shown as gray data points) show a steeper downturn toward the noise level than the median stack of $z > 5.7$ quasars from E. P. Farina et al. (2019) shown in teal. In the case of J158–14, the surface brightness profile seems to suggest that the extent of the nebula might continue below the noise level, which is not surprising given that this quasar seems to have a much longer lifetime than the lifetime revealed by its PZ.

Additionally, this method assumes that the dominant mechanism behind the observed extended Lyα emission is the recombination of a free electron with an ionized hydrogen atom. This assumption has been supported by studies at lower redshift (C. N. Leibler et al. 2018; V. Langen et al. 2023) that compared the extended Lyα emission to the extended Hα emission around quasars and found a close agreement with recombination based on their respective line fluxes. However, it should be noted that Lyα can in general also arise from resonant scattering, which can alter the velocity profile of its emission. The presence of scattering as the Lyα photons make their way from the BLR to and through the CGM would thus result in an increased light travel time that we are currently not accounting for. T. Costa et al. (2022) have shown that resonant scattering increases the asymmetries and also the velocity dispersion in the nebular Lyα line profiles. Our measured velocity dispersions (Table 2) are in line with the values

[11] Note that the last gray data point for J0330–4025 in Figure 4 is slightly elevated; this is due to a few higher-SNR patches in the field that have not been identified to be a part of this quasar's nebula; see the middle panel of Figure 1.

expected for recombination radiation from T. Costa et al. (2022), although the asymmetries and low spectral resolution of the line profiles shown in Figure 3 make it difficult to draw any definite conclusions. This limitation motivates further deep integral-field-unit observations of the rest-frame optical lines where resonant scattering is suppressed (e.g., Hα, [O III]) to enable a more complete picture of nebular quasar lifetimes.

In summary, our results show that the nebular quasar lifetimes from extended Lyα emission are consistent with the existing PZ-based lifetimes, assuming recombination radiation is the dominant emission mechanism. This result disfavors the scenario where time-variable obscuration effects would have led to short measured UV-luminous quasar lifetimes. This finding provides further support that these $z \sim 6$ quasars could have started their accretion only recently, but a study of their rest-frame optical emission is needed for more conclusive evidence and investigation into alternative SMBH growth pathways.

Acknowledgments

We would like to thank the referee for the comments that improved the quality of this manuscript. We would also like to thank Roberto Decarli and Bram Venemans for the helpful discussions.

E.P.F. is supported by the international Gemini Observatory, a program of NSF NOIRLab, which is managed by the Association of Universities for Research in Astronomy (AURA) under a cooperative agreement with the U.S. National Science Foundation, on behalf of the Gemini partnership of Argentina, Brazil, Canada, Chile, the Republic of Korea, and the United States of America. R.A.M. acknowledges support from the Swiss National Science Foundation (SNSF) through project grant 200020_207349. C.M. acknowledges support from Fondecyt Iniciacion grant 11240336 and the ANID BASAL project FB210003.

Based on observations collected at the European Southern Observatory under ESO programs 106.215A, 108.222J, 0101.A-0656, 0103.A-0562, and 297.A-5054.

Appendix A
How Fast Do Lyα Nebulae Grow?

The method presented in Section 4 uses the light-crossing time of the ionized nebula as the relevant timescale to convert the size of the nebula to a quasar lifetime constraint. This works if the Lyα nebula itself grows at or close to the speed of light when the quasar radiation turns on. In what follows, we demonstrate that this is the case for typical CGM conditions around quasars and for timescales relevant to this work.

The CGM is known to be a highly inhomogeneous, multiphase medium. Lyα nebulae are primarily thought to be powered through the hydrogen recombination cascade (C. N. Leibler et al. 2018; V. Langen et al. 2023) and trace the denser, colder neutral gas clouds within the CGM, with typical number densities of $n_{\rm H} \approx 1{\rm cm}^{-3}$ (S. Cantalupo et al. 2014; F. Arrigoni Battaia et al. 2015; J. F. Hennawi et al. 2015). However, the volume filling factor of these neutral gas clouds is generally small, $C_{\rm V} < 10^{-2}$ (M. McCourt et al. 2018; G. Pezzulli & S. Cantalupo 2019), and can be as low as $C_{\rm V} \sim 10^{-5}$–10^{-4} (J. X. Prochaska & J. F. Hennawi 2009). Such tiny values of $C_{\rm V}$ imply that most of the gas in the CGM is ionized, enabling the ionizing photons to travel at the speed of light until they encounter a neutral patch along their line of sight. In other words, the observed Lyα nebulae simply trace the sightlines that illuminate these small, dense neutral gas clouds, and the light travel time to the farthest illuminated gas cloud should thus accurately reflect the quasar lifetime.

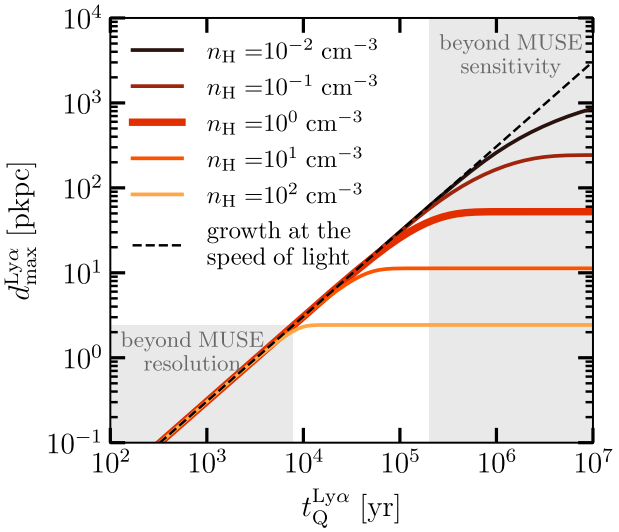

Figure 6. The growth of the ionized Lyα nebula size, $d_{\rm max}^{{\rm Ly}\alpha}$, as a function of quasar lifetime, $t_{\rm Q}^{{\rm Ly}\alpha}$, following the relativistic treatment of P. R. Shapiro et al. (2006) for a range of hydrogen number densities, $n_{\rm H}$. For typical densities of $n_{\rm H} \approx 1$ cm^{-3} (thick curve) that are responsible for Lyα nebulae (S. Cantalupo et al. 2014; F. Arrigoni Battaia et al. 2015; J. F. Hennawi et al. 2015), the expansion of the nebula size closely follows the speed of light (dashed line) up to $t_{\rm Q}^{{\rm Ly}\alpha} \sim 10^5$ yr. This is actually a lower bound on the range of lifetimes our method is valid for, as in a more realistic, mostly ionized CGM with a low volume filling factor of neutral gas clouds, the ionization front would move close to the speed of light out to even larger distances.

One might still object that, even though the photons travel at the speed of light through the CGM until they hit a neutral gas cloud, the time it takes to photoionize this residual neutral gas could be limiting the speed at which nebulae can grow. To address this concern, we proceed to demonstrate that the ionization front travels at or close to the speed of light through gas under conditions relevant for Lyα emission and for timescales relevant to this work.

We consider a toy model where we assume that the CGM around the quasar is homogeneous and only composed of neutral hydrogen gas at a constant number density $n_{\rm H}$. Note that this simple model will yield the most pessimistic estimate on how fast the ionization front progresses through the CGM due to the increased rate of recombinations in a fully neutral medium. Following the treatment of relativistic ionized fronts in P. R. Shapiro et al. (2006; Equations (30)–(36) therein), we compute the size of the ionized nebula, $d_{\rm max}^{{\rm Ly}\alpha}$, around a typical quasar of luminosity $L = 10^{47}\,{\rm erg\,s^{-1}}$ as a function of the quasar lifetime, $t_{\rm Q}^{{\rm Ly}\alpha}$, for a range of hydrogen number densities $n_{\rm H}$ typically considered in relevant literature (e.g., F. Arrigoni Battaia et al. 2015). We plot the results in Figure 6 as solid curves at a range of colors (the thick curve highlighting the typical value $n_{\rm H} = 1\,{\rm cm^{-3}}$) alongside a dashed line depicting growth at the speed of light.

From Figure 6, we can see that even if the quasar had to carve out an ionized bubble in this unrealistic fully neutral CGM model, the growth of this ionized region would still progress close to the speed of light up until $t_{\rm Q}^{{\rm Ly}\alpha} \sim 10^5$ yr from the moment the quasar has turned on. This result implies

that for all of our measurements in this manuscript, the light travel time to the edge of the nebula is indeed a good tracer of the actual quasar lifetime, especially given that the quasar only needs to photoionize small neutral gas clouds instead of the whole CGM.

Two further points can be made here. First, note that the lifetime of $t_{\rm Q}^{{\rm Ly}\alpha} \sim 10^5$ yr also corresponds roughly to the limit of what we can constrain with our observations, as the predicted surface brightness profile would fall below the sensitivity achieved with MUSE for longer lifetimes (see Figure 4). Second, in the parameter space that is inaccessible due to the limited spatial resolution of MUSE, the nebula would grow close to the speed of light for all $n_{\rm H}$ values considered in our toy model. This means that we can actually place an upper bound on the lifetimes of quasars whose Lyα nebulae are not detected in deep MUSE observations as, even if their growth were limited by the speed of the ionization front, their nebulae should be expanding at the speed of light even in the densest parts of the CGM.

Appendix B
Spectral Regions

In Figures 7 and 8, we display the extracted spectrum for each quasar in our sample as well as the spectral regions that have been used to search for foreground sources (in blue), to extract the PSF (in purple), and, if detected, the region where extended nebular emission was found (in orange; corresponding to the median nebula as described in Section 3). The vertical dashed line marks the Lyα emission of the quasar corresponding to the systemic redshift from Table 1. These figures also show the spectral channels that have been masked due to having large surface brightness uncertainty, strong sky line emission, or residual detector artifacts (as described in Section 3; displayed as faint vertical gray lines).

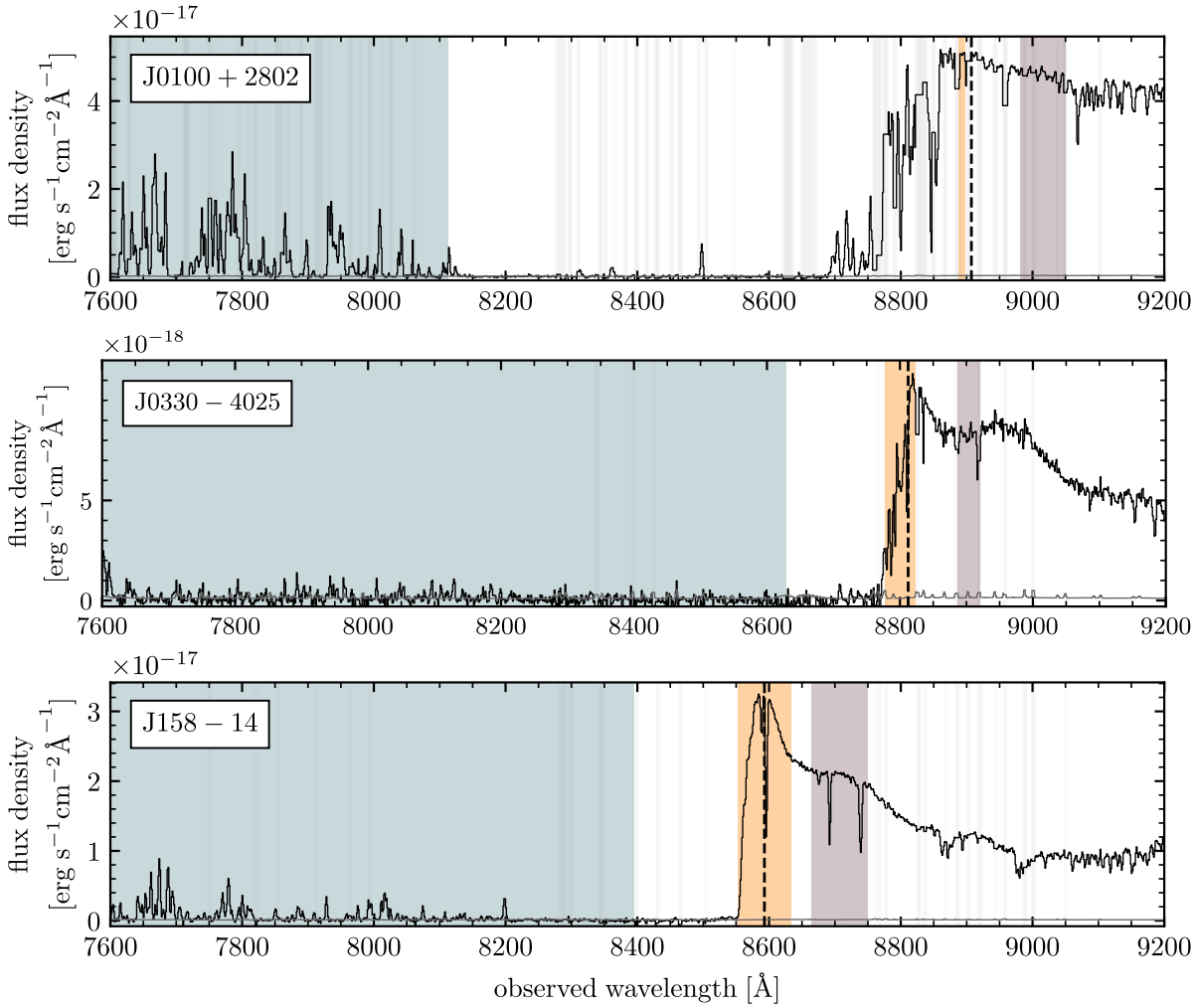

Figure 7. Spectral regions corresponding to the wavelengths where foreground sources are identified (in blue; foreground defined as 5× the size of the quasar's PZ blueward of Lyα), where PSF is extracted (in purple), and where nebular emission is detected (in orange). The black data in each row show the quasar spectrum extracted from the MUSE data cube using an aperture with a radius of three pixels, with the error vector displayed in gray. The vertical dashed line marks Lyα corresponding to the quasar's systemic redshift given in Table 1, and the faint gray vertical lines show the spectral channels that have been masked as described in Section 3.

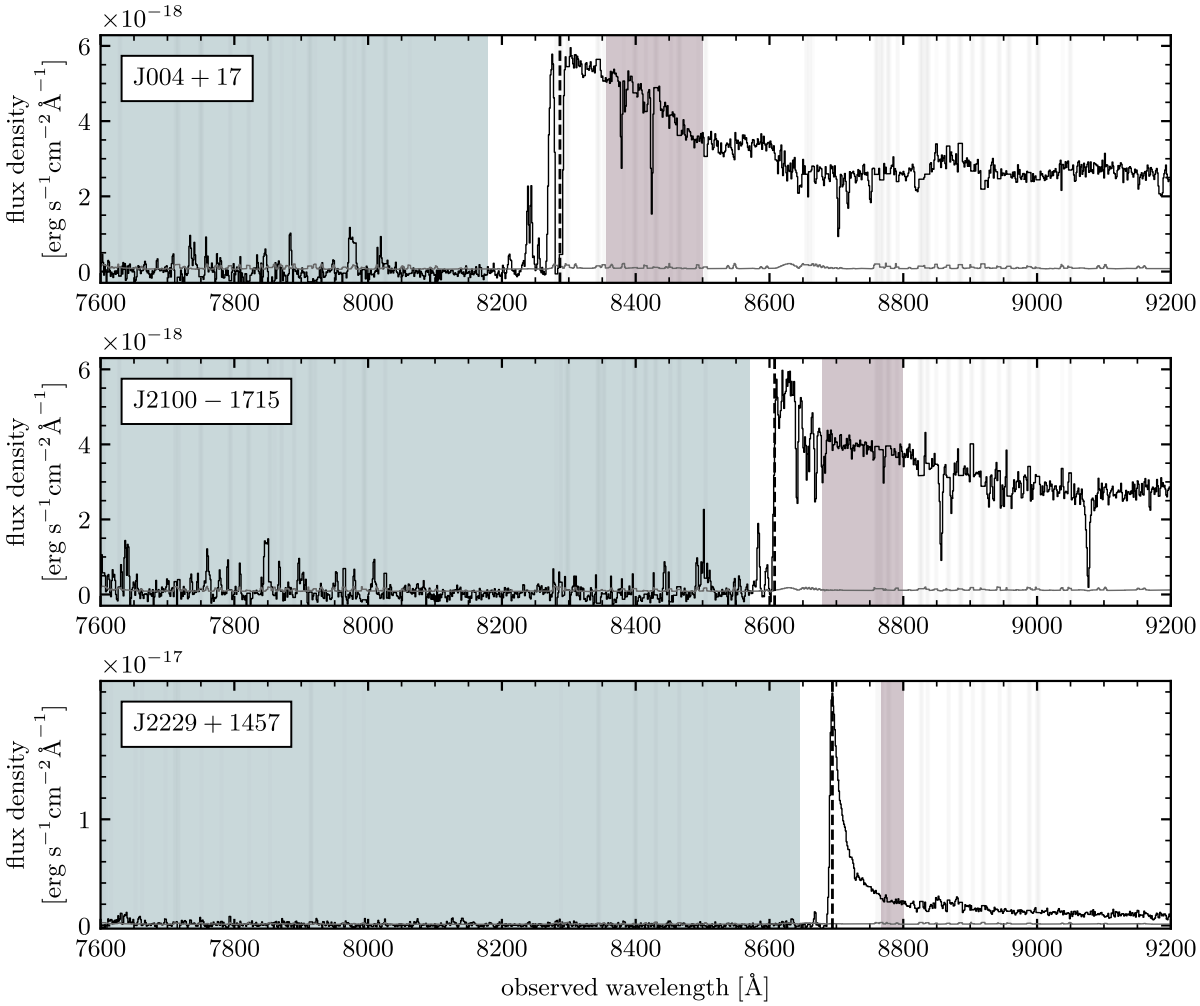

Figure 8. Same as Figure 7 but for quasars without a nebular detection.

ORCID iDs

Dominika Ďurovčíková https://orcid.org/0000-0001-8986-5235
Anna-Christina Eilers https://orcid.org/0000-0003-2895-6218
Romain A. Meyer https://orcid.org/0000-0001-5492-4522
Emanuele Paolo Farina https://orcid.org/0000-0002-6822-2254
Eduardo Bañados https://orcid.org/0000-0002-2931-7824
Frederick B. Davies https://orcid.org/0000-0003-0821-3644
Joseph F. Hennawi https://orcid.org/0000-0002-7054-4332
Chiara Mazzucchelli https://orcid.org/0000-0002-5941-5214
Robert A. Simcoe https://orcid.org/0000-0003-3769-9559
Fabian Walter https://orcid.org/0000-0003-4793-7880

References

Arrigoni Battaia, F., Hennawi, J. F., Cantalupo, S., & Prochaska, J. X. 2016, ApJ, 829, 3
Arrigoni Battaia, F., Hennawi, J. F., Prochaska, J. X., et al. 2019, MNRAS, 482, 3162
Arrigoni Battaia, F., Yang, Y., Hennawi, J. F., et al. 2015, ApJ, 804, 26
Bacon, R., Accardo, M., Adjali, L., et al. 2010, Proc. SPIE, 7735, 773508
Bacon, R., Brinchmann, J., Richard, J., et al. 2015, A&A, 575, A75
Bañados, E., Venemans, B. P., Mazzucchelli, C., et al. 2018, Natur, 553, 473
Borisova, E., Cantalupo, S., Lilly, S. J., et al. 2016b, ApJ, 831, 39
Borisova, E., Lilly, S. J., Cantalupo, S., et al. 2016a, ApJ, 830, 120
Cantalupo, S., Arrigoni-Battaia, F., Prochaska, J. X., Hennawi, J. F., & Madau, P. 2014, Natur, 506, 63
Christensen, L., Jahnke, K., Wisotzki, L., & Sánchez, S. F. 2006, A&A, 459, 717
Connor, T., Bañados, E., Cappelluti, N., & Foord, A. 2024, Univ, 10, 227
Costa, T., Arrigoni Battaia, F., Farina, E. P., et al. 2022, MNRAS, 517, 1767
Davies, F. B., Hennawi, J. F., & Eilers, A.-C. 2019, ApJL, 884, L19
Davies, F. B., Wang, F., Eilers, A.-C., & Hennawi, J. F. 2020, ApJL, 904, L32
Drake, A. B., Farina, E. P., Neeleman, M., et al. 2019, ApJ, 881, 131
Ďurovčíková, D., Eilers, A.-C., Chen, H., et al. 2024, ApJ, 969, 162
Ďurovčíková, D., Eilers, A.-C., Simcoe, R. A., et al. 2025, ApJL, 987, L33
Eilers, A.-C., Davies, F. B., Hennawi, J. F., et al. 2017, ApJ, 840, 24
Eilers, A.-C., Hennawi, J. F., & Davies, F. B. 2018, ApJ, 867, 30
Eilers, A.-C., Hennawi, J. F., Davies, F. B., & Simcoe, R. A. 2021, ApJ, 917, 38
Eilers, A.-C., Hennawi, J. F., Decarli, R., et al. 2020, ApJ, 900, 37
Eilers, A.-C., Mackenzie, R., Pizzati, E., et al. 2024, ApJ, 974, 275
Fan, X., Bañados, E., & Simcoe, R. A. 2023, ARA&A, 61, 373
Farina, E. P., Arrigoni-Battaia, F., Costa, T., et al. 2019, ApJ, 887, 196
Farina, E. P., Venemans, B. P., Decarli, R., et al. 2017, ApJ, 848, 78
Gunn, J. E., & Peterson, B. A. 1965, ApJ, 142, 1633
Heckman, T. M., Lehnert, M. D., Miley, G. K., & Van Breugel, W. 1991a, ApJ, 381, 373
Heckman, T. M., Miley, G. K., Lehnert, M. D., & Van Breugel, W. 1991b, ApJ, 370, 78
Hennawi, J. F., & Prochaska, J. X. 2013, ApJ, 766, 58
Hennawi, J. F., Prochaska, J. X., Cantalupo, S., & Arrigoni-Battaia, F. 2015, Sci, 348, 779

Inayoshi, K., Visbal, E., & Haiman, Z. 2020, ARA&A, 58, 27
Johnson, J. L., & Bromm, V. 2007, MNRAS, 374, 1557
Langen, V., Cantalupo, S., Steidel, C. C., et al. 2023, MNRAS, 519, 5099
Leibler, C. N., Cantalupo, S., Holden, B. P., & Madau, P. 2018, MNRAS, 480, 2094
Mackenzie, R., Pezzulli, G., Cantalupo, S., et al. 2021, MNRAS, 502, 494
Martin, D. C., Chang, D., Matuszewski, M., et al. 2014, ApJ, 786, 107
McCourt, M., Oh, S. P., O'Leary, R., & Madigan, A.-M. 2018, MNRAS, 473, 5407
Morey, K. A., Eilers, A.-C., Davies, F. B., Hennawi, J. F., & Simcoe, R. A. 2021, ApJ, 921, 88
Pezzulli, G., & Cantalupo, S. 2019, MNRAS, 486, 1489
Pizzati, E., Hennawi, J. F., Schaye, J., et al. 2024, MNRAS, 534, 3155
Planck Collaboration, Aghanim, N., Akrami, Y., et al. 2020, A&A, 641, A6
Prochaska, J. X., & Hennawi, J. F. 2009, ApJ, 690, 1558
Satyavolu, S., Eilers, A.-C., Kulkarni, G., et al. 2023b, MNRAS, 522, 4918
Satyavolu, S., Kulkarni, G., Keating, L. C., & Haehnelt, M. G. 2023a, MNRAS, 521, 3108
Shapiro, P. R., Iliev, I. T., Alvarez, M. A., & Scannapieco, E. 2006, ApJ, 648, 922
Soltan, A. 1982, MNRAS, 200, 115
Soto, K. T., Lilly, S. J., Bacon, R., Richard, J., & Conseil, S. 2016, MNRAS, 458, 3210
Tanaka, T., & Haiman, Z. 2009, ApJ, 696, 1798
Trainor, R., & Steidel, C. C. 2013, ApJL, 775, L3
Volonteri, M., & Rees, M. J. 2006, ApJ, 650, 669
Wang, F., Davies, F. B., Yang, J., et al. 2020, ApJ, 896, 23
Wang, F., Yang, J., Fan, X., et al. 2021, ApJL, 907, L1
Weilbacher, P. M., Streicher, O., Urrutia, T., et al. 2012, Proc. SPIE, 8451, 84510B
Weilbacher, P. M., Streicher, O., Urrutia, T., et al. 2014, 485, 451
Whalen, D., van Veelen, B., O'Shea, B. W., & Norman, M. L. 2008, ApJ, 682, 49
Wu, X.-B., Wang, F., Fan, X., et al. 2015, Natur, 518, 512
Yu, Q., & Tremaine, S. 2002, MNRAS, 335, 965
Yue, M., Eilers, A.-C., Simcoe, R. A., et al. 2023, ApJ, 950, 105
Zhou, Y., Chen, H., Matteo, T. D., et al. 2024, MNRAS, 528, 3730